Phonon dispersion relations and softening in photoexcited bismuth from first principles

É. D. Murray,[1] S. Fahy,[1,2] D. Prendergast,[3] T. Ogitsu,[3] D. M. Fritz,[2] and D. A. Reis[2]
[1]*Tyndall National Institute and Department of Physics, University College, Cork, Ireland*
[2]*FOCUS Center, University of Michigan, Ann Arbor, Michigan 48109-1040, USA*
[3]*Lawrence Livermore National Laboratory, P.O. Box 808, Livermore, California 94550, USA*
(Received 11 October 2006; revised manuscript received 13 February 2007; published 2 May 2007)

The phonon dispersion relations for equilibrium and photoexcited bismuth are calculated from first-principles density-functional perturbation theory, with constrained occupation of excited electronic states. The dependence of phonon frequency on photoexcited electron-hole plasma density is found for modes throughout the Brillouin zone. The resulting phonon dispersion curves are in good agreement with available neutron-scattering data for the equilibrium occupation of electronic bands. We find the effect of phonon softening by the electron-hole plasma to be substantially larger in the optical modes than in the acoustic modes throughout the Brillouin zone.

DOI: 10.1103/PhysRevB.75.184301 PACS number(s): 63.20.Dj, 63.20.Kr, 78.47.+p

I. INTRODUCTION

Developments in pump-probe optical spectroscopy using powerful femtosecond pulsed lasers now allow direct time-domain investigations of phonon motion and electron-phonon coupling.[1] Bismuth has been the focus of many studies of high amplitude coherent phonon generation.[2–6] Other materials such as antimony[3] and tellurium[3,7] have also shown some similar behavior. The effects of these very short, intense laser pulses and of the resulting excited electron-hole plasma on materials are not well understood. The aim of this work is to provide a better understanding of the electron and phonon dynamics involved in ultrafast pump-probe experiments on the picosecond time scale.

Previous work on laser-induced electron-hole plasmas in Si and GaAs (Refs. 8–10) found, using a phenomenological model for the cohesive energy, that the zone-boundary acoustic modes in these semiconductors became unstable in the excited system. This was also found in more recent work on Si (Ref. 11) using density-functional perturbation theory with a finite temperature Fermi-Dirac distribution to incorporate the effects of electronic excitation. In this work, we use first-principles electronic structure methods to calculate the effect of photoexcitation on the phonon dispersion curves in bismuth for densities of photoexcited carriers up to 1% of the valence electron density per unit cell. We use a constrained density-functional theory approach, which has provided results in good agreement with experiment for the zone-center longitudinal-optical (A_{1g}) mode in previous work on bismuth.[12,13] Our approach differs from that of Ref. 11 in the representation of the excited system; we represent the photoexcited distribution on the time scale of a typical pump-probe experiment ($\sim$ picosecond), assuming it to be much shorter than a typical electron-hole recombination time ($\sim$ nanosecond[14]). The calculations are performed using a version of the open-source density-functional theory (DFT) code ABINIT,[15,16] in which we have implemented the constrained DFT method. In contrast with tetrahedrally bonded semiconductors, we obtain no significant softening of the acoustic modes in photoexcited bismuth, making its behavior more similar to that of Al.[11]

The equilibrium unit-cell structure of bismuth is rhombohedral A7 (Ref. 17). The direction of the trigonal axis is usually chosen as the z axis. There are two atoms in the unit cell, the second located a fractional distance x along the trigonal axis, as shown in Fig. 1. In its equilibrium configuration (in the ground electronic state), $x=0.468\ 14$. If x were 0.5, i.e., halfway along the trigonal axis, and α were 60°, this would be a simple cubic structure with one atom per cubic unit cell. The observed deviation from cubic symmetry is caused by a Peierls distortion. It is because of the existence of this Peierls distortion that the equilibrium bismuth struc-

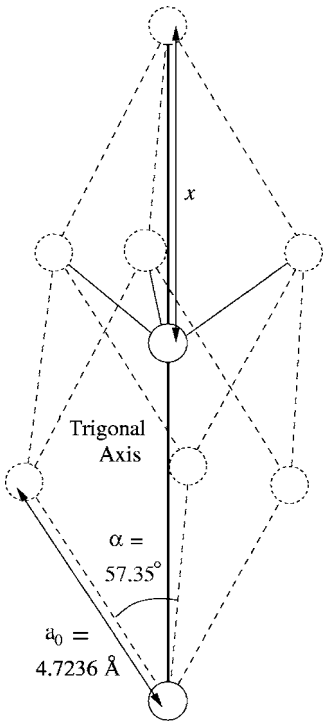

FIG. 1. Bismuth atomic structure with experimental lattice parameters taken from Ref. 20. The bold line marks the trigonal axis, the dashed lines mark out the unit cell, while the remaining solid lines indicate the bonding. The two atoms in a primitive unit cell are shown as solid circles, while adjacent atoms are dashed.

ture is very sensitive to the excitation of electrons to higher bands. When electrons are moved to higher bands, the energetic advantage of the off-symmetry structure is reduced, causing relaxation toward the more symmetric configuration, i.e., the value of x shifts toward 0.5 with increased excitation. This process is evident in ultrafast pump-probe experiments on bismuth, where an intense pump pulse excites electrons from the valence to the conduction bands, causing changes in the atomic equilibrium positions and restoring forces as described, so that the atoms oscillate about their new equilibria. This allows for the generation of large-amplitude coherent phonons by displacive excitation,[3,18] a mechanism that is a special case of stimulated Raman scattering involving an imaginary component of the susceptibility.[19] In ultrafast pump-probe experiments, oscillations of the A_{1g} mode are detected, corresponding to the variation of the parameter x.

We begin this paper with a description of the theoretical approach used in the calculations. This includes discussions of constrained density-functional theory, density-functional perturbation theory (DFPT),[21–24] and a description of the alterations needed to standard DFPT to incorporate the constrained DFT approach and apply it to photoexcited systems. Section III then gives details of the computational scheme used for the calculations presented here. Section IV gives our main results. This includes a comparison of phonon frequencies calculated from both the DFPT method and the frozen-phonon method, the DFPT dispersion curves for the nonexcited system compared with neutron-scattering experiments, and the predicted dispersion curves for the photoexcited system. The conclusions of this work are discussed in Sec. V.

II. THEORY

A. Constrained density-functional theory

Constrained density-functional theory[25,26] has been developed to allow first-principles calculations to be performed on photoexcited systems in which the electron-hole recombination time is longer than the typical phonon period. In a pump-probe experiment, the primary effect of the pump pulse on the time scale of interest in phonon motion is the creation of an excited distribution of electrons within the bands. In our approach, the intraband scattering rate is assumed to be much faster than the time scale of interest in pump-probe experiments, allowing the electrons and holes to relax into a Fermi-Dirac distribution while remaining within the conduction or valence bands. Constrained DFT calculations have been used to replicate this effect by separately constraining the total occupations of the valence bands and conduction bands. Bismuth, while normally termed a semimetal, has less than 2×10^{-5} free carriers per unit cell,[17] allowing it to be treated effectively as a zero-band-gap semiconductor. The valence and conduction bands are filled independently of each other using Fermi-Dirac distributions, the chemical potentials of which are determined by requiring the correct total number of electrons within each set of bands separately. It is in this way that a constrained DFT calculation differs from the standard DFT method. This allows the total energy to be calculated for a constant density of free carriers, n, excited to the conduction bands and has been previously shown to accurately predict the phonon softening of the zone-center modes in photoexcited tellurium[25,26] and bismuth.[12]

Zone-center mode frequencies can be calculated with constrained DFT using the frozen-phonon technique. To do this, a finite amplitude displacement of atoms is "frozen" into the system for a fixed excited electron-hole plasma density and the resulting energy calculated directly. To calculate the A_{1g} frequency in bismuth, for example, the total energy is calculated for a range of values of x about its equilibrium and the phonon frequency is then found from the resulting curvature. This approach has also been used to investigate the effect of anharmonicity of the A_{1g} phonon in bismuth.[12] The interatomic potential-energy surface for photoexcited bismuth calculated using this method has been shown to be in excellent agreement with recent experimental measurements.[13]

B. Density-functional perturbation theory

DFPT (Refs. 21, 22, and 27) allows the response of the electronic system to an applied perturbation to be calculated self-consistently from first principles. It has many applications,[24] such as calculating the result of the application of an electric field or the effect of a strain on a system. When the perturbing potential arises from the displacement of the atomic positions, the interatomic force matrix can be calculated and the phonon frequencies are obtained from the resulting dynamical matrix. The principal advantage of the DFPT approach to calculating phonon frequencies is that the workload of the calculation is independent of the phonon wavelength, as the responses to perturbations of different wavelengths are decoupled. This is in contrast to the frozen-phonon method, which requires the use of large supercells to calculate phonon frequencies for long-wavelength phonons.

C. DFPT for photoexcited systems

In order to apply DFPT to photoexcited systems, we have combined it with constrained DFT. Constrained DFT is quite similar in implementation to Fermi-Dirac smearing for metals.[23] In standard Fermi-Dirac smearing, there is a single Fermi energy, determined by normalization to the total number of electrons; in our constrained DFT, there are two independent chemical potentials, one for conduction bands and one for valence bands, determined by the number of excited electron-hole pairs required. We follow the treatment for DFPT in metals as implemented for non-zone-center phonons in ABINIT, the theory behind this being well described in Sec. II C 4 of Ref. 24. This method is altered to handle a system with two chemical potentials instead of the single Fermi level used in Fermi-Dirac smearing. We find the changes in state occupations and total energy that result from a perturbation of atomic positions, while using the constrained occupation as described in Sec. II A. This occurs as changes in the atomic positions will lead to changes in the calculated energy levels of the system, which will then lead to changes in the filling of these levels within the Fermi-Dirac distributions used in the constrained DFT method. This leads to the need to calculate the first-order variation in the density. This is given in Eq. (68) of Ref. 24. As this work is

focused on the calculation of non-zone-center phonons, the second term in this equation vanishes; as in the metallic case, the chemical potentials are unaffected by the perturbation to linear order for $q \neq 0$. As described in Ref. 24, the expression for the variation in the density can be written as

$$\Delta n(\mathbf{r}) = R_{n,m}\psi_n^*(\mathbf{r})\psi_m(\mathbf{r})\langle\psi_m|\Delta V_{SCF}|\psi_n\rangle,$$

where $R_{n,m}=(\tilde{\theta}_{F,n}-\tilde{\theta}_{F,m})/(\epsilon_n-\epsilon_m)$. The difference between the standard Fermi-Dirac smearing calculation and our constrained occupation calculation arises in the accurate calculation of $R_{n,m}$. It can be calculated directly when ϵ_n and ϵ_m differ sufficiently, but its limit must be found whenever $\epsilon_m \rightarrow \epsilon_n$. This limit is calculated via the analytic calculation of the derivative of the occupation with respect to the energy of each band. In our system, this is the derivative with respect to ϵ_n of the Fermi-Dirac distribution function at state n, and is given by

$$D_n = -\frac{\exp\left(\frac{\epsilon_n-\mu_i}{\sigma}\right)}{\sigma\left[1+\exp\left(\frac{\epsilon_n-\mu_i}{\sigma}\right)\right]^2},$$

where the subscript n refers to the band in question, while the subscript i indicates that the value of the chemical potential μ depends on whether n is a valence band or a conduction band. The required ratio, $R_{n,m}$, is then found as the average of this derivative calculated explicitly at each of the bands n and m, $\frac{1}{2}(D_n+D_m)$, in the calculation. All other aspects of the calculation can proceed as in the Fermi-Dirac smearing case.

III. COMPUTATIONAL SCHEME

The open-source code ABINIT (Refs. 15 and 16) was used for the calculations. The calculation of linear response for ground-state systems, including metals, has already been fully implemented in the code. It was then altered to make use of the constrained DFT approach for photoexcited systems as described in Sec. II C. All the calculations were performed using the Hartwigsen-Goedecker-Hutter pseudopotential[28] for bismuth, including spin-orbit coupling, and the local-density approximation to exchange and correlation. An energy cutoff of 15 hartree was used in the plane-wave expansion of wave functions and four shifted $8\times8\times8$ Monkhurst-Pack k point grids were used for the Brillouin-zone integration. For the photoexcited system, the temperature k_BT for the Fermi-Dirac distribution was fixed at 0.5 eV. For this value, the average energy per electron-hole pair is equal to the incident photon energy (1.5 eV) in a typical pump-probe experiment.[12]

The minimum-energy lattice parameters for the ground-state system were found by structural optimization using the Broyden-Fletcher-Goldfarb-Shanno minimization.[29] The lattice parameters obtained in this manner differ slightly from the experimental values quoted in Sec. I, with $a_0=4.695$ Å and $\alpha=57.56°$. The equilibrium value of x was found for each excitation density, while keeping the lattice parameters fixed at the values obtained for the ground state, as their variation would correspond to a change in the volume of the crystal as a whole, which cannot occur on the time scale of ultrafast pump-probe experiments. The relation between x and the level of excitation obtained from our calculations is shown in Fig. 2. We then performed a linear-response calculation,[30,31] where the dynamical matrix is found by calculating the second-order derivatives of the energy with respect to ionic displacements (see Sec. II C of Ref. 24), and the phonon frequencies are obtained as the square root of its eigenvalues.

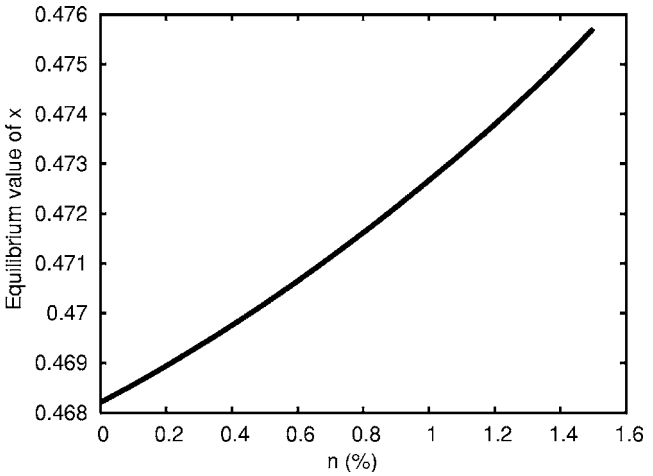

FIG. 2. Variation of the internal cell parameter, x, as a function of the fraction, n, of valence electrons excited to the conduction bands.

The dynamical matrices of a grid of four shifted $4\times4\times4$ phonon wave vectors were calculated using ABINIT. The dynamical matrices are interpolated by taking the Fourier transform to find the real-space interatomic force constants using the ANADDB program from the package. It is then possible, by taking the inverse Fourier transform at the desired wave vector, to obtain the dynamical matrix, and hence phonon frequencies, for any phonon in the Brillouin zone.

IV. RESULTS

A. Comparison to frozen-phonon results

Frozen-phonon calculations were performed for both the excited and unexcited systems for the modes at the T point in the Brillouin zone, using a supercell of double the primitive unit-cell size, in order to compare these results with those obtained from the linear-response method. In both of these methods, the temperature of the Fermi-Dirac distribution is constrained to be constant when calculating the phonon frequency. The results from both approaches for both the ground and excited states are shown in Table I. The differences between both methods are small in all cases. The partial filling of bands in the $n=1\%$ case gives rise to a greater sensitivity to Brillouin-zone sampling and a greater discrepancy between the frozen-phonon and linear-response results.

TABLE I. Comparison of frozen-phonon (FP) results with linear-response (LR) results for calculations of mode frequencies at the T point. n is the fraction of the valence electrons excited to the conduction bands. All frequencies are in THz.

	$n=0\%$		$n=1\%$	
	LR	FP	LR	FP
TA	1.161	1.161	1.191	1.183
LA	1.759	1.758	1.771	1.765
TO	2.994	2.994	2.795	2.800
LO	3.232	3.231	3.068	3.061

B. Ground state

Figure 3 shows how the calculated dispersion curves for the ground-state system compare to experimental inelastic-neutron-scattering results.[32,33] It is clear that most of the experimental optical- and acoustic-mode frequencies are well reproduced in the calculations, with the largest difference on the order of 5%, for the TO mode at Γ. It should be noted, however, that the work of Smith[33] shows poor agreement for the mode in the binary direction labeled b in Fig. 3. All other calculated modes agree well with his results (see Fig. 3, Γ-K-X line). The behavior we calculate for this mode is in agreement with the inelastic-neutron-scattering results of MacFarlane, as shown in Ref. 34. Along the binary direction, Smith has obtained two acoustic modes quite close together in a frequency region, where our calculations predict a single acoustic mode. This may have occurred due to difficulty in resolving mixed longitudinal and transverse modes along the binary direction in the experiments, as the agreement between theory and experiment is otherwise excellent. The eigenvectors for modes propagating in the binary direction

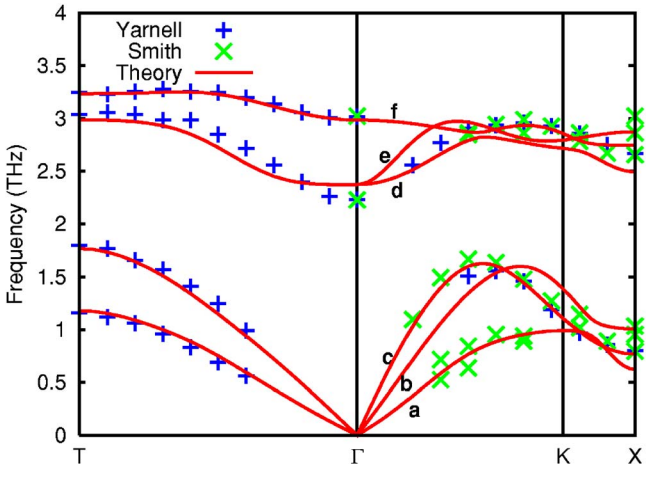

FIG. 3. (Color online) Calculated dispersion curves for the ground state (red lines) compared to the experimental neutron-scattering results of Yarnell *et al.* (Ref. 32) (blue+signs) and Smith (Ref. 33) (green × signs) for phonons in the trigonal direction (T to Γ in the first Brillouin zone) and in the binary direction (Γ to X of an adjacent Brillouin zone, passing through the zone boundary at K). The labels a–f are discussed in the text.

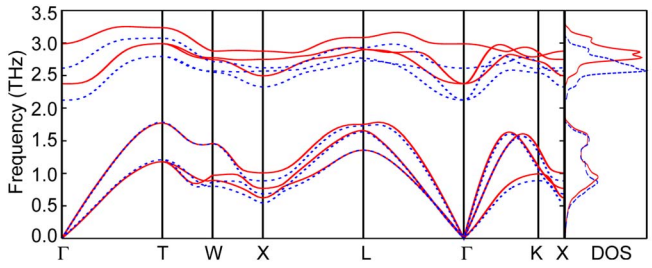

FIG. 4. (Color online) Phonon dispersion curves and density of states calculated for both the ground and excited states. Results are shown for $n=0\%$ (red solid) and $n=1\%$ (blue dashed), where n is the fraction of the valence electrons excited to the conduction bands.

have two distinct symmetries, with the modes labeled c, d, and f in Fig. 3 being symmetric under twofold rotation about the wave-vector direction, while those labeled a, b, and e are antisymmetric under twofold rotation about this direction. We find that modes along this direction show significant mixing of longitudinal and transverse behaviors. The modes labeled a and b are almost pure transverse-acoustic modes near the Γ point along this direction, but show an increasing mixing of longitudinal-optical behavior away from the Γ point. The mode labeled b shows significantly more variation, becoming almost completely longitudinal optical in the region near the K point, and returning to transverse acoustic in the region near the X point. The mode labeled a remains primarily transverse acoustic in the region near the K point, but becomes longitudinal optical as it approaches the X point. The mode labeled c begins as longitudinal acoustic near the Γ point, but its behavior is almost entirely transverse optical near the K point and remains as such near the X point.

C. Excited state

The dispersion curves calculated for both 0% and 1% of the valence electrons excited to the conduction bands are shown in Fig. 4. We obtain a value of 2.61 THz for the A_{1g} frequency at 1%, compared to a value of 2.51 THz obtained in the experiments described in Ref. 13. It is evident that the acoustic modes are largely unaffected by the photoexcitation of electrons, with the only significant change near the X point, while there is a noticeable reduction in all the optical-mode frequencies. This reduction is almost uniform throughout the Brillouin zone, although the largest softening occurs for the LO mode at the zone center, where the reduction in frequency is approximately twice that which occurs away from the zone center. This is also seen in the phonon density of states, shown in Fig. 4. The peak at higher frequency, corresponding to the optical modes, is almost uniformly reduced in frequency, while the peak corresponding to the acoustic modes shows little change.

In order to investigate the nature of the bond softening evident, the interatomic force constants obtained were examined. For each pair of interacting atoms, a 3×3 force tensor is obtained, with elements corresponding to movement of each of the atoms along the Cartesian directions. In order to give a measure of the strength of this interaction, we use the

TABLE II. Comparison of the trace of the interatomic force constant tensor (in units of 10^{-3} hartree/bohr^2), between pairs of atoms as labeled in Fig. 5, along with the distances between the atoms (in bohr units) for $n=0\%$ and $n=1\%$ of the valence electrons excited into the conduction bands. The trace for the fifth and seventh nearest-neighbor pairs is negligible and is omitted.

		IFC Trace		Distance	
Pair	NN	$n=0\%$	$n=1\%$	$n=0\%$	$n=1\%$
A	First	−33.23	−27.74	5.766	5.807
B	Second	−0.88	−0.52	6.604	6.552
C	Third	−0.67	−0.86	8.544	8.544
D	Fourth	−0.30	−0.50	8.873	8.873
E	Sixth	−0.26	−0.16	10.360	10.439
F	Eighth	−0.43	−0.26	11.766	11.687
G	Ninth	−4.16	−4.40	12.318	12.318

trace of the interatomic force constant tensor. This property is directly connected to the phonon frequencies[35] and has the advantage of being independent of the coordinate system used. Table II and Fig. 5 show the changes in the trace of the interatomic force constant tensor for some of the different pairs of atoms available. They show that the strongest interaction is with the nearest-neighbor atoms, and this reduces markedly in magnitude going from $n=0\%$ to $n=1\%$. The second strongest interaction is between the pair of atoms labeled "G". This interaction shows a slight increase in magnitude in the photoexcited case.

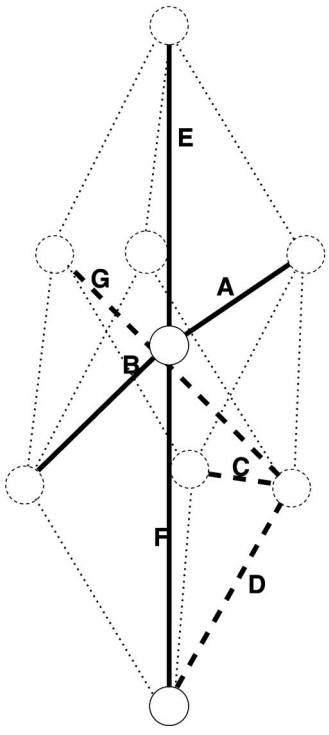

FIG. 5. Pairs of bismuth atoms labeled in Table II where the trace of interatomic force constant tensor, and distance between the atoms, is listed for both the unexcited and excited system. The dashed line joining the pairs marked C, D, and G indicates that, unlike the other marked pairs, these pairs are between an atom in the primitive unit cell and its equivalent atom in an adjacent unit cell. These distances depend only on the lattice parameters and are thus fixed at their values for the unexcited system, as described in Sec. III. The dotted line shows the unit-cell outline.

Two main factors contribute to the softening of modes in the excited case. First, the bond strength itself is reduced by moving electrons out of their bonding states. Second, as the equilibrium moves toward $x=0.5$, the optical modes must tend toward their corresponding acoustic modes, as the system moves from a two atom unit cell to a single atom unit cell system. To show the relative importance of each of these contributions to the resulting mode softening, the phonon dispersion curve for the unexcited system was calculated with the second atom fixed at the equilibrium value of x found for $n=1\%$ of the valence-band electrons excited into the conduction bands. In this way, the contribution to the mode softening from the change in x alone can be seen. The resulting dispersion curves are shown, together with the original $n=0\%$ and $n=1\%$ calculations, in Fig. 6. The resulting curve for the LO mode falls approximately halfway between the original $n=0\%$ and $n=1\%$ calculations. This indi-

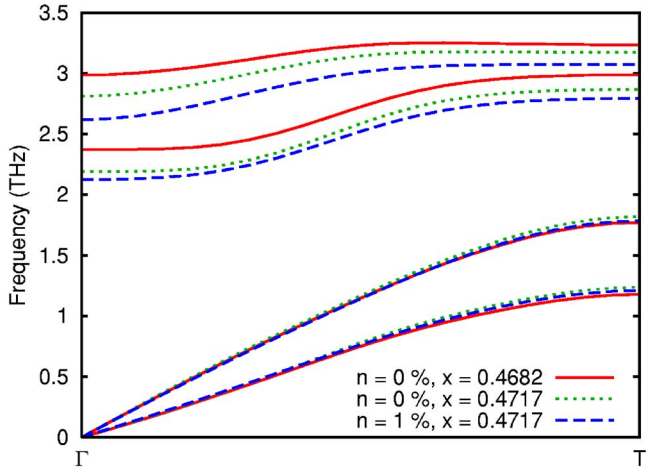

FIG. 6. (Color online) Phonon dispersion curves for $n=0\%$, $x(n=0\%)$ (red solid); $n=1\%$, $x(n=1\%)$ (blue dashed); and $n=0\%$, $x(n=1\%)$ (green dotted).

cates a roughly equal contribution to the softening coming from the excitation of electrons and the change in the equilibrium value of x. The dispersion curves for the TO modes, which are degenerate between Γ and T, fall quite close to the original $n=1\%$ curves. This would indicate that the change in the equilibrium value of x in the excited case is the dominating factor in the softening of the TO modes.

V. CONCLUSIONS

We have demonstrated a method to calculate phonon softening throughout the Brillouin zone in a photoexcited material. Photoexcitation of bismuth causes an almost uniform reduction in the optical-mode frequencies, while the acoustic modes are largely unaffected. This result is explained by an analysis of the changes in the interatomic force constants induced by photoexcitation. The optical modes are primarily governed by interactions between the two different atoms in the unit cell, while acoustic modes are largely determined by interactions between an atom in the unit cell and its corresponding atom in nearby unit cells. We find that interactions of the first type are reduced noticeably in magnitude on photoexcitation, in contrast with those of the second type, which show a slight increase.

ACKNOWLEDGMENTS

This work was supported by the Irish Research Council for Science, Engineering and Technology, funded by the National Development Plan, by Science Foundation Ireland and by the U.S. National Science Foundation FOCUS Physics Frontier Center. Part of the work was performed under the auspices of the U.S. Department of Energy at the University of California/LLNL under Contract No. W-7405-Eng-48. The calculations were performed using the LC machine "Thunder" at LLNL.

[1] R. Merlin, Solid State Commun. **102**, 207 (1997).
[2] T. K. Cheng, S. D. Brorson, A. S. Kazeroonian, J. S. Moodera, G. Dresselhaus, M. S. Dresselhaus, and E. P. Ippen, Appl. Phys. Lett. **57**, 1004 (1990).
[3] T. K. Cheng, J. Vidal, H. J. Zeiger, G. Dresselhaus, M. S. Dresselhaus, and E. P. Ippen, Appl. Phys. Lett. **59**, 1923 (1991).
[4] M. F. DeCamp, D. A. Reis, P. H. Bucksbaum, and R. Merlin, Phys. Rev. B **64**, 092301 (2001).
[5] M. Hase, K. Mizoguchi, H. Harima, S. Nakashima, M. Tani, K. Sakai, and M. Hangyo, Appl. Phys. Lett. **69**, 2474 (1996).
[6] K. Sokolowski-Tinten, C. Blome, J. Blums, A. Cavalleri, C. Dietrich, A. Tarasevitch, I. Uschmann, E. Förster, M. Kammler, M. Horn-von-Hoegen *et al.*, Nature (London) **422**, 287 (2003).
[7] S. Hunsche, K. Wienecke, T. Dekorsy, and H. Kurz, Phys. Rev. Lett. **75**, 1815 (1995).
[8] R. Biswas and V. Ambegaokar, Phys. Rev. B **26**, 1980 (1982).
[9] P. Stampfli and K. H. Bennemann, Phys. Rev. B **46**, 10686 (1992).
[10] P. Stampfli and K. H. Bennemann, Phys. Rev. B **49**, 7299 (1993).
[11] V. Recoules, J. Clérouin, G. Zérah, P. M. Anglade, and S. Mazevet, Phys. Rev. Lett. **96**, 055503 (2006).
[12] É. D. Murray, D. M. Fritz, J. K. Wahlstrand, S. Fahy, and D. A. Reis, Phys. Rev. B **72**, 060301(R) (2005).
[13] D. M. Fritz, D. A. Reis, B. Adams, R. A. Akre, J. Arthur, C. Blome, P. H. Bucksbaum, A. L. Cavalieri, S. Engemann, S. Fahy *et al.*, Science **315**, 633 (2007).
[14] J. Shah, *Ultrafast Spectroscopy of Semiconductors and Semiconductor Nanostructures*, Springer Series in Solid State Sciences Vol. 115 (Springer, Berlin, 1996).
[15] X. Gonze, J.-M. Beuken, R. Caracas, F. Detraux, M. Fuchs, G.-M. Rignanese, L. Sindic, M. Verstraete, G. Zerah, F. Jollet *et al.*, Comput. Mater. Sci. **25**, 478 (2002).
[16] The ABINIT code is a common project of the UniversitÃ© Catholique de Louvain, Corning Incorporated, and other contributors (http://www.abinit.org).
[17] X. Gonze, J.-P. Michenaud, and J.-P. Vigneron, Phys. Rev. B **41**, 11827 (1990).
[18] H. J. Zeiger, J. Vidal, T. K. Cheng, E. P. Ippen, G. Dresselhaus, and M. S. Dresselhaus, Phys. Rev. B **45**, 768 (1992).
[19] T. E. Stevens, J. Kuhl, and R. Merlin, Phys. Rev. B **65**, 144304 (2002).
[20] D. Shiferl and C. S. Barret, J. Appl. Crystallogr. **2**, 30 (1969).
[21] S. Baroni, P. Giannozzi, and A. Testa, Phys. Rev. Lett. **58**, 1861 (1987).
[22] X. Gonze, Phys. Rev. A **52**, 1096 (1995).
[23] S. de Gironcoli, Phys. Rev. B **51**, 6773 (1995).
[24] S. Baroni, S. de Gironcoli, A. Dal Corso, and P. Giannozzi, Rev. Mod. Phys. **73**, 515 (2001).
[25] P. Tangney and S. Fahy, Phys. Rev. Lett. **82**, 4340 (1999).
[26] P. Tangney and S. Fahy, Phys. Rev. B **65**, 054302 (2002).
[27] E. N. Zein, Sov. Phys. Solid State **26**, 1825 (1984).
[28] C. Hartwigsen, S. Goedecker, and J. Hutter, Phys. Rev. B **58**, 3641 (1998).
[29] J. E. Dennis, Jr. and R. B. Schnabel, *Numerical Methods for Unconstrained Optimization of Nonlinear Equations* (Prentice-Hall, Englewood Cliffs, NJ, 1983).
[30] X. Gonze, Phys. Rev. B **55**, 10337 (1997).
[31] X. Gonze and C. Lee, Phys. Rev. B **55**, 10355 (1997).
[32] J. L. Yarnell, J. L. Warren, R. G. Wenzel, and S. H. Koenig, IBM J. Res. Dev. **8**, 234 (1964).
[33] D. B. Smith, Los Alamos Report No. 3773, 1967 (unpublished).
[34] *Non-Tetrahedrally Bonded Elements and Binary Compounds I*, Landolt-Börnstein New Series, Group III, Vol. 41, Pt. C (Springer, 1998).
[35] A. J. E. Foreman and W. M. Lomer, Proc. Phys. Soc. London, Sect. B **70**, 1143 (1957).